Investigation of Crystal Shape Controllability in the Micro-Pulling-Down Method for Low-Wettability Systems

Rikito Murakami,* Katsunari Oikawa, Kei Kamada, and Akira Yoshikawa

ACCESS | Metrics & More | Article Recommendations

ABSTRACT: This study presents the criteria for shape control in the micro-pulling-down (μ-PD) method for low-wettability systems (dewetting μ-PD method), which enables us to achieve highly shape-controllable crystal growth. In the dewetting μ-PD method, the presence of the die wall inhibits the direct observation of the meniscus during the process. Therefore, in this study, the meniscus shape was calculated using the Young−Laplace equation to predict the optimal crystal growth conditions. The free-end and fixed-end boundary conditions to be satisfied for the differential equations were defined at the triple point, with the melt on the die wall. The relationship between the crystal diameter and pressure in the fixed-end condition, wherein the wetting angle (α) at the triple point of the crystal was 90°, indicated the suppression of the melt infiltration by the presence of crystals. The gap between the die and crystal was minimized for the contact angle (θ) and growth angle (α_{gr}) in the fixed-end and free-end conditions, at which $|\alpha_{gr} + \theta - \pi|$ was minimum at a given pressure under the assumption of single-valued solutions. The results of this study will facilitate the formation of noble-metal alloys with a net shape and expand the scope for the development of new materials.
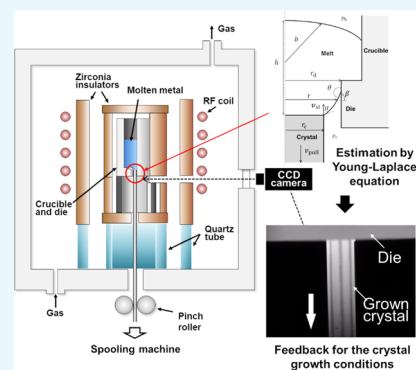
1. INTRODUCTION

The capillary shaping technology (CST) is defined as the process of achieving shape-controlled solidification of a melt using surface tension. It is widely used for the growth of semiconductor crystals and single crystals of high-melting-point oxides.[1−6] The different techniques for CST include the Czochralski method, floating zone method, and micro-pulling-down (μ-PD) method. These techniques are classified based on the positional relationship between the crystal, melt, and object that holds the melt. In the μ-PD method, a seed crystal is brought into contact with a crucible with a hole at the bottom and gently drawn down to produce a single crystal, such as sapphire. The μ-PD method is exclusively utilized to grow small crystals with dimensions less than the capillary constant at high speeds (0.1−2 mm min^{-1}) and can be applied to oxides, halides, and alloys by selecting the appropriate crucible material and die shape.[2,6−15] There are numerous combinations of a low-wettability melt with a complementary die, where the contact angle θ is larger than $\pi/2$, such as carbon crucibles with fluoride phosphors[11] and ceramic crucibles with shape memory alloys.[15] In the case of low-wettability systems, the melt does not pass through the capillary spontaneously without sufficient pressure, and solidification occurs inside the capillary, which cannot be seen directly. Meanwhile, the solidification interface can be directly observed in the case of the conventional μ-PD method. Therefore, to keep the crystal diameter constant, we aimed to derive the necessary condition by calculating the capillary

geometry with several parameters (e.g., pressure, crystal diameter, and contact angles at the crystal and die wall).

Figure 1 shows a schematic diagram of the μ-PD method using a ceramic crucible. The metallic material that is set in the crucible is melted by high-frequency induction heating. The seed crystals are brought into contact with the crucible through a hole at its bottom and gradually recrystallized, which results in continuous unidirectional solidification. The hole part of the crucible is distinguished as a die (or shaper). The state of the crystals underneath the die is observed using charge-coupled devices and additional techniques because it is impossible to observe the meniscus directly. The crystal shape is regulated by controlling the pulling rate and the output of a high-frequency oscillator that changes the temperature of the melt. This technique of producing metallic crystals using a ceramic crucible was recently referred to as the alloy-μ-PD (A-μ-PD) method.[12,15]

In recent times, we fabricated long wires of iridium ($T_{m.p.}$ = 2447 °C) and the iridium−rhodium alloy ($T_{m.p.} \approx 2150$ °C) and demonstrated their utility as thermocouples.[15] The
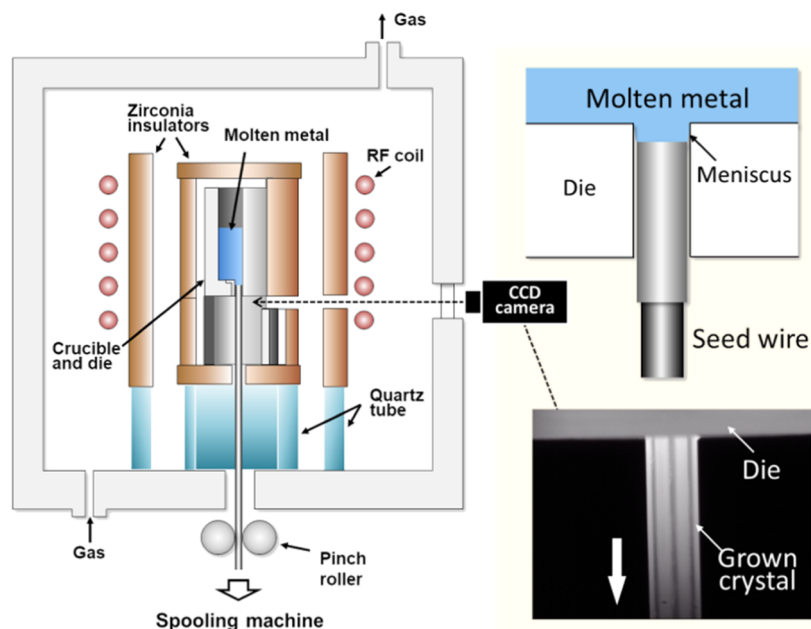
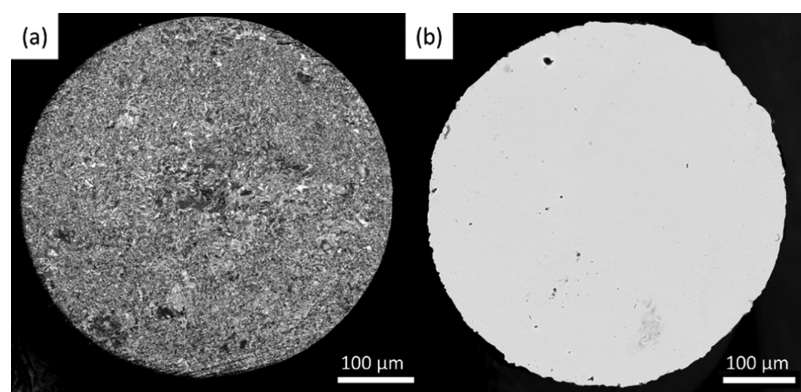**Figure 1.** Schematic of the μ-PD method using a ceramic crucible.

Figure 2. Cross section of an iridium wire with a diameter of 0.5 mm. (a) Mechanically processed commercial wire. (b) As-grown iridium wire.

microstructural differences between the mechanically processed wire and the grown iridium wire were shown by scanning electron microscopy (S-3400N, Hitachi) images of their cross sections (Figure 2a,b). A channeling contrast owing to the difference in the crystal orientation was observed in the processed commercial product; furthermore, the wires comprised fine crystal grains that were several micrometers in size (Figure 2a). Conversely, the grown iridium wire comprised single-crystal grains (Figure 2b).

The grown iridium wires exhibited high flexibilities owing to the monocrystalline structure and were not susceptible to degradation induced by the grain boundaries.[15] Therefore, they can be utilized for novel applications, such as thermocouple wires. Furthermore, the demonstration of a forming process for precious metals expands the scope of development of materials for medical stents and various diverse applications. It has been confirmed that the crystal size uncertainty during the shape-controlled solidification of iridium and iridium−rhodium alloys can be limited within ±30 μm even at a pulling-down rate of 999 mm min^{-1} (the maximum speed of the apparatus) under certain conditions. The conventional μ-PD method cannot be utilized to achieve such shape controllability because the melt is exposed to the external environment. Therefore, the effects

of melt wettability and the inner wall in the dewetting μ-PD method should be distinguished from those in the conventional μ-PD method. This study demonstrated the dewetting μ-PD method, wherein the solidification interface was located inside the hole in a low-wettability system. Furthermore, the dewetting μ-PD method was distinguished from the conventional μ-PD method, wherein the free surface was not constrained by the wall.

The melt spontaneously passes through the capillary and forms droplets at the tip of the die in high-wettability systems, such as the combination of an iridium crucible with sapphire. Because the droplets are exposed to the external environment outside the crucible, shape-controlled solidification can be easily achieved by directly observing the solidification interface after seeding and adjusting the heating power. However, the melt does not spontaneously penetrate at pressures below the threshold pressure in low-wettability systems. This can be attributed to the repulsion owing to the surface tension at the edge of the die wall. Therefore, seeding is performed either by applying a pressure that is higher than the threshold pressure or by bringing the seed into contact with the melt in the crucible. The solidification interface is located inside the crucible and cannot be directly observed, except in the case of

a transparent vessel. Therefore, it is difficult to experimentally optimize the parameters to achieve shape controllability for fluoride and high-melting-point metals, such as iridium; moreover, quartz crucibles are not compatible with these materials. There have been extensive experiments and simulations on the μ-PD method in high-wettability systems, and the crystal diameter for specific crystal growth conditions has been successfully determined for such systems.[16,17] However, there are limited quantitative studies on shape controllability and the phenomena underlying shape controllability in the μ-PD method for low-wettability systems.

Previous studies on the CST in low-wettability systems demonstrated the techniques of pulling from shaper (TPS) method for the growth of Ge and GaAs ribbon-shaped crystals under microgravity[18] and the Bridgman method with gas pressure control for the growth of GaSb crystals.[19−21] The Bridgman method has been studied in detail to determine the conditions for maintaining a constant gap between the crystal and the wall surface in a given growth environment. These investigations are based on the capillary geometry that is characterized by the contact angle, θ, and the growth angle, α. A moderate gap between the capillary wall and the inner wall of the container during solidification can smooth the surface in low-wettability systems; furthermore, it can markedly decrease the dislocations that are induced in the crystal owing to the difference in the coefficients of thermal expansion of the capillary and container walls.[22]

Shape controllability ($< \pm$ 20 μm) is typically required for the industrial application of the dewetting μ-PD method to ensure that the variation in diameter is limited to within 2% for a crystal with a diameter of 1 mm. This is equivalent to the shape controllability that is achieved by the existing plastic working methods, such as wire drawing. However, it is difficult to suppress the vibrations at the crystal growth interface, which are induced by the environment and operation of the equipment during crystal growth, to a few micrometers over a long period of time. Therefore, it was focused on how the gap width with the die reduced by shape control in the dewetting μ-PD method. In this work, shape controllability in the dewetting μ-PD method was analyzed from the viewpoint of the capillary geometry, and the relevance of shape controllability to the experimentally observed behavior and the applicability of the process were discussed.

2. FORMULATION AND NUMERICAL CALCULATION

The two common issues associated with CST are the determination of the meniscus shape and dynamic stability of the meniscus against small disturbances. The dynamic stability has been analyzed by various techniques[1,23,24] and is often discussed in different contexts. In CST, the focus is often on the triple point on the crystal side and whether or not the crystal diameter continues to decrease with solidification. Tatarchenko[1,18] used Lyapunov's stability analysis to determine the dynamic stability of methods such as TPS and Bridgman. When an equilibrium state exists in a given dynamic system with numerous parameters and the time variation of the deviation from the equilibrium state is within a certain range, a system is considered to be dynamically stable; a detailed explanation is provided in the literature. For example, Tatarchenko[1,18] analyzed the TPS and Bridgman methods with two independent variables: the diameter of the crystal (r) and the height of the solidification interface (h).

Figure 3 shows the schematic diagram and parameters of the dewetting μ-PD method near the solid−liquid interface. Both
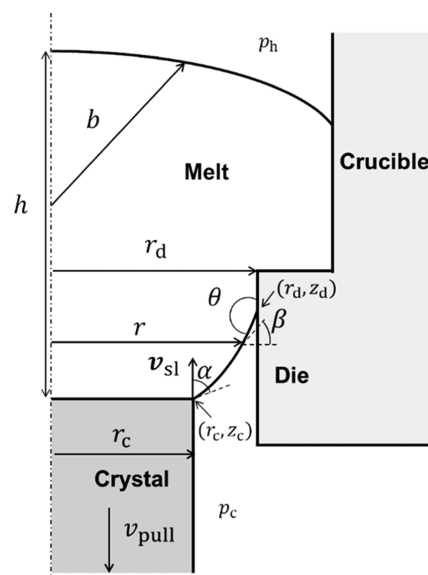

Figure 3. Parameters and placement in the dewetting μ-PD method.

the fixed-end and free-end conditions in the dewetting μ-PD method can be obtained, as described later. The depiction shows that in both boundary conditions, the parameters characterizing the system can be expressed by r and h, respectively. This is similar to the representations of the TPS and Bridgman methods by the same two parameters, r and h, in the fixed-end and free-end conditions, respectively.

2.1. Configuration of the Crystal Growth. The dynamic stability of the capillary in the height direction of a system with n = 2 is expressed by the equation for the thermal balance in association with solidification. When the conditions for the thermodynamic stability are satisfied, the variation in deviation of the solidification interface from the equilibrium point converges within a certain range. However, the effect of heat transfer on parameters, such as the surface tension, is negligible in the environments where the effect of gravity is insignificant, that is, regions of a low Bo number.[1] The radial dynamic stability in such regions is expressed by the following equation

$$v_{sl}\left(\frac{d\alpha_0}{dr}\right)_{r_c} < 0 \tag{1}$$

where v_{sl} is the velocity of movement at the solid−liquid interface, α_{gr} is the growth angle, r is the radial coordinate, and r_c is the crystal radius. The μ-PD method is usually applicable at scales below the capillary constant. Therefore, the Bo number is less than 1, and the conditions for the thermodynamic stability are always assumed to be satisfied to simplify the calculations in this study.

The shape of the meniscus at the static state is obtained from the variational principle of minimizing the surface energy, assuming that the volume of the liquid is constant, and is typically described by the Young−Laplace equation. The Young−Laplace equation, in this study, is considered in the form of an arc-length parameter, s, assuming an axisymmetric field. The equations are normalized by the hole radius, r_d. The advantage of this form, described by three first-order ordinary differential equations, is that the solution is uniquely

determined for the initial conditions using the Cauchy–Lipschitz theorem

$$\frac{dr}{ds} = \cos \beta$$

$$\frac{dz}{ds} = \sin \beta$$

$$\frac{d\beta}{ds} = -\frac{\sin \beta}{r} + (dP - Boz) \qquad (2)$$

The dimensionless parameters are as follows

$$r = \frac{r^*}{r_d}, \qquad z = \frac{z^*}{r_d}, \qquad \beta(r^*) \to \beta^*(r),$$

$$s = \frac{s^*}{r_d}$$

$$\Delta P \equiv \frac{dp r_d}{\gamma_{lv}}, \qquad dp \equiv p_h + \rho g h + \frac{2\gamma_{lv}}{b} - p_c$$

$$Bo = \frac{\rho_l g r_d^2}{\gamma_{lv}}$$

where z is the height, s is the arc-length parameter, β is the angle of the capillary tangent with respect to the horizontal direction, p_h and p_c are the pressures applied to the top and bottom of the melt, respectively, ρ is the melt density, g is the acceleration due to gravity, h is the melt height, γ_{lv} is the surface tension of the melt, and b is the radius of curvature at the top of the melt. The pressure difference between the upper and lower surfaces of the capillary section can be neglected ($p_h - p_c = 0$) because the dewetting μ-PD method is usually applied in an open system. It should be noted that $p_h - p_c$ does not become 0 during the application of pressure (in a closed system).

ΔP includes the positive or negative effects of the surface tension above the melt and the Lorentz force on the melt during induction heating. It also includes the negative effects of the loss in the frictional pressure owing to the withdrawal and inflow resistances during the inflow of the melt. The inflow resistance and frictional loss in the capillary are of the order of a few pascals even if the pulling rate reaches up to a few hundred millimeters for iridium crystals with a diameter of 1 mm. Therefore, the inflow resistance and frictional loss in the capillary were excluded from direct examination in this study.

2.2. Boundary Conditions. The two boundary conditions in the dewetting μ-PD method are presented in Figure 4a. The free-end condition exists at the inner wall of the die, wherein the melt tip maintains a constant θ with the inner wall. The fixed-end condition exists at the inner edge of the die, wherein the Gibbs condition allows the variation of θ in the range of $\pi - \varphi$ (Figure 4b). In the quasi-static state, θ is often approximated by the equilibrium contact angle θ_e. The transition from the fixed-end condition to the free-end condition occurs at the advancing contact angle, θ_a, while the transition from the free-end condition to the fixed-end condition occurs at the receding contact angle, θ_r. This can be attributed to the presence of hysteresis in the contact angle. The most basic shape in this study is represented by $\varphi = 90°$ with $\pi/2 \leq \theta \leq \pi$. When the triple point at the inner wall comes in contact with the lower edge of the die, there is a transition from the free-end condition to the fixed-end
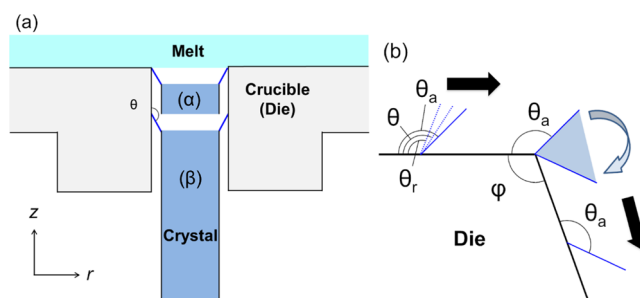

Figure 4. (a) Schematic of the boundary conditions in the dewetting μ-PD method. (α) Fixed-end condition and (β) free-end condition. (b) Range of variation in the contact angle in the fixed-end condition in the case that the triple point moves to one direction.

condition. Consequently, the meniscus is no longer constrained by the inner wall of the die. Therefore, observation of the meniscus was excluded from the scope of this study as it falls within the scope of studies on the conventional μ-PD method.

The solutions in the fixed-end condition were obtained using MATLAB from $s = 0$ to the value of s that satisfied the condition, $\beta(s = s_{end}) = \frac{\pi}{2} - \alpha$, for a given ΔP and Bo number.

$$z(s = 0) = 0, \qquad r(s = 0) = r_d,$$

$$\beta(s = 0) = \theta - \frac{\pi}{2}$$

Similar solutions were obtained in the free-end condition and for an arbitrary r_c from $s = 0$ to the value of s that satisfied the condition, $\beta(s = s_{end}) = \theta - \frac{\pi}{2}$. Thus, the following initial conditions were obtained

$$z(s = 0) = 0, \qquad r(s = 0) = r_c,$$

$$\beta(s = 0) = \frac{\pi}{2} - \alpha$$

Previous studies on the meniscus shape under free-end conditions demonstrated the dynamic stability of the shape against minor changes in the crystal radius even for solutions that contained multiple inflection points and melt heights more than 10 times the hole radius.[25] However, among other methods, the floating zone method indicates that the limit of the capillary height is denoted as the Rayleigh limit, which is 2π times the crystal radius, from the viewpoint of the rupture of the liquid column.[26] Therefore, in this study, the investigation of the dewetting μ-PD method includes only practically meaningful solutions, wherein z was single-valued with respect to r, under the condition that $r < r_d$ is always satisfied owing to the presence of the wall surface.

The growth angle, α_{gr}, was determined from the balance of the surface energy at the triple point of the crystal, the melt, and the gas. It is expressed by the following equation[27]

$$\alpha_{gr} = \arccos\left(\frac{\gamma_{lg}^2 + \gamma_{sg}^2 - \gamma_{sl}^2}{2\gamma_{lg}\gamma_{sg}}\right) \qquad (3)$$

The growth angle in the steady state, wherein crystal growth progresses with a constant diameter, is defined as the angle between the growth direction vector of the solid phase and the tangential vector of the liquid interface, where α (apparent contact angle) $= \alpha_{gr}$. The apparent contact angle between the

melt and the crystal can be defined at the triple point on the crystal side, which can be regarded as a fixed end owing to hysteresis,[17] and the meniscus shape for $\alpha \neq \alpha_{gr}$ is determined under the assumption that the fixed-end condition is satisfied at (r_c, z_c).

The specific materials that were assumed in this study included a zirconia crucible and a system of iridium and ruthenium. Multiple physical properties were utilized for the calculations (Table 1). The density and surface tension of the

Table 1. Physical Properties of Iridium and Ruthenium

physical properties	iridium	ruthenium
melting point T_m [K]	2720[28]	2607[30]
liquid density ρ [kg/m³]	19,509[29]	10,739[31]
surface tension γ [N/m]	2.230[29]	2.254[31]
growth angle α_{gr} [deg]	variable	variable
capillary constant a [m]	0.0048	0.0065

molten materials were calculated at the melting points, T_m, of both iridium and ruthenium. The growth angle was variable because its exact values were unknown. The contact angles of iridium and ruthenium to the yttria-stabilized zirconia (YSZ) are yet to be reported. We measured the contact angle of iridium and ruthenium on YSZ as a reference value after the droplets (1 mm in diameter) formed on the lid by the steam from the crucible solidified during heating in a reduced pressure, high-purity Ar atmosphere. The contact angles of iridium and ruthenium on YSZ were approximately 120−130°. Ruthenium showed a slightly lower contact angle than iridium. In this study, $\theta = 130°$ was assumed to be the contact angle. Contact angles in this range are common for non-reactive metal melts and ceramics and not specific to this system. The capillary constant, a, is expressed as $\sqrt{2\gamma/\rho g}$.

3. RESULTS AND DISCUSSION

3.1. Depiction of the Fixed-End Conditions. The steady state of crystal growth in the dewetting μ-PD method was achieved under the fixed-end conditions. When the decrease in volume of the melt in the crucible was negligible, the capillary shape was uniquely defined in the fixed-end condition because the position of the solidification interface remained unchanged. Furthermore, the crystal size remained constant during stable growth, that is, (r_c, z_c) was constant and α was equal to α_{gr}. Figure 5 shows the meniscus shape and envelope for a typical fixed-end condition. Herein, $\alpha = 5°$, $\Delta P = 0.7–2.1$, $Bo = 0.021$, and $\theta = \sim 90–180°$. Under the fixed-end conditions, the triple point on the crystal side moved along the envelope according to the value of θ, and the meniscus shape changed accordingly.

The dynamic stability in the radial direction was examined by calculating the change in α with a slight change in r_c. Figure 5a,b shows the meniscus curves and their envelopes for $\Delta P = 0.7$ and 2.0, respectively, for the growth of an iridium crystal under the assumption that $\pi/2 \leq \theta \leq \pi$. The Bo number and α_{gr} were assumed to be 0.0215 and 5°, respectively. It is known that there is a switch in the dynamic stability/instability around the vertex of the envelope for a low Bo number.[32] Therefore, the conditions for dynamic stability were satisfied on the die side ($r_c \approx 0.6$) and not on the center side of the envelope for the vertex (Figure 5a). These observations conformed with the results obtained by Tatarchenko,[18,32] which showed that dynamic stability could be obtained for $r_c > 0.7$ in the TPS method for liquids with a low Bo number. Furthermore, the conditions for dynamic stability were consistently satisfied for the concave meniscus (Figure 5b).

3.2. Depiction of the Free-End Conditions. When the melt infiltrated into the hole and the triple point increased along the wall as a non-stationary condition, the free-end condition in the dewetting μ-PD method was obtained. The characteristics of the free-end condition were similar for the dewetting μ-PD and Bridgman methods. However, the triple point continued to increase with the crystal growth in the Bridgman method, whereas the range of movement of the triple point was limited by the edge inside the die in the dewetting μ-PD method.

Low-wettability melts do not spontaneously infiltrate at pressures below the threshold pressure. Therefore, the z-coordinate at the die side z_d was fixed, and the transition to the free-end condition was impossible. The pressure of the melt that was flowing into the through hole was denoted as the critical pressure for the transition from the fixed-end condition to the free-end condition in the absence of the seed crystal. The relationship between the infiltration pressure and height of the melt (h), with respect to the hole radius, is shown in Figure 6; here, it was assumed that the hydrostatic pressure was the only influence on the melt. When $\theta = 130°$, the melt (height = 0.5 cm) did not leak from a hole with a diameter of 2 mm, that is, the fixed-end condition was maintained

$$\Delta P_{inf} = -\frac{2\gamma_{lv} \cos\theta}{r_d} \frac{r_d}{\gamma_{lv}} = -2\cos\theta \qquad (4)$$

When crystals were present inside the hole, it was difficult to elucidate the mechanism of melt infiltration using only the capillary. This was because the position of the triple point on the crystal side changed dynamically depending on the temperature field. The position of the triple point was determined by the total heat balance between the heating of
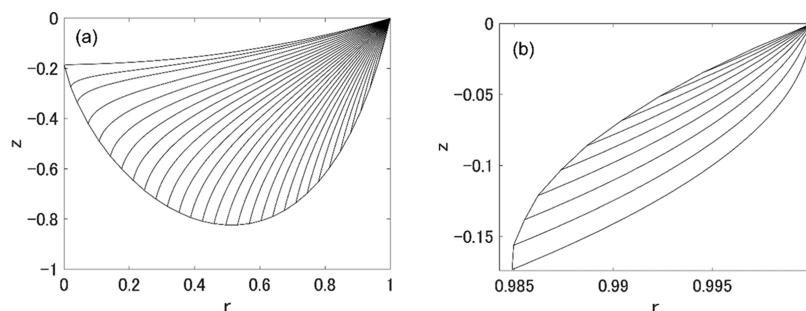

Figure 5. Typical capillary shapes and envelopes with (a) vertex and (b) concave meniscus.
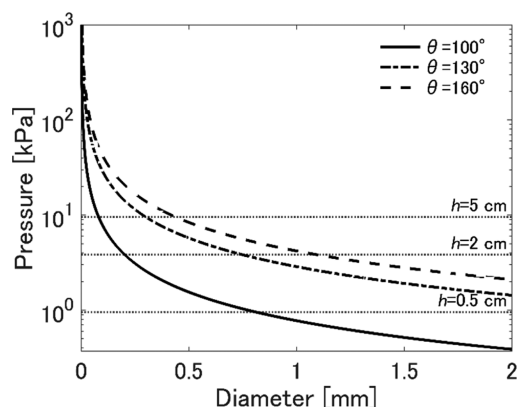
Figure 6. Relationship between the hole radius and infiltration pressure for different heights of the iridium melt.

the melt and heat transfer in the melt, crystal, and thermal insulators. Therefore, the gap width could not be simply predicted. From an industrial perspective, it was worth considering the application of a certain amount of pressure to increase the crystal diameter and to achieve shape controllability. However, an excessively high pressure results in leakage of the melt. Melt infiltration is sometimes used in the seeding process with thin seed crystals. Therefore, it was useful to consider the pressure range at which melt leakage did not occur in relation to the crystal diameter.

The lowest height of the capillary interface was equal to the triple point at the solid−liquid interface, that is, α was 90° for the determination of the dimensionless critical pressure for infiltration, ΔP_{inf}. When the crystal exists in the hole, ΔP_{inf} can be obtained as ΔP, where α is 90° in the fixed-end condition. Figure 7a shows the dependence of α and ΔP on the different crystal diameters for iridium. Here, θ is assumed to be 130° for a hole diameter of 0.3 mm.

Figure 7a shows that the pressure at $\alpha = 90°$ ($\alpha + \theta = 220°$) is obtained at the inflection point of each curve and converges to a constant value as r_c approaches 0.

Figure 7b shows the dependence of ΔP_{inf} on r_c at $\alpha = 90°$. The pressure at $r_c = 0$ was approximately $\Delta P_{inf} = 1.286$, while the inflow pressure, ΔP_{inf}, was 1.282 at $r_c \rightarrow 0$ (Figure 7b). The slight difference was attributed to the consideration of weight of the capillary section in the calculated values using the Young−Laplace equation.

When r_c approached r_d, owing to the increase in the crystal diameter, there was a sharp increase in the infiltration pressure above approximately $r_c = 0.8$ (Figure 7b). This indicated a
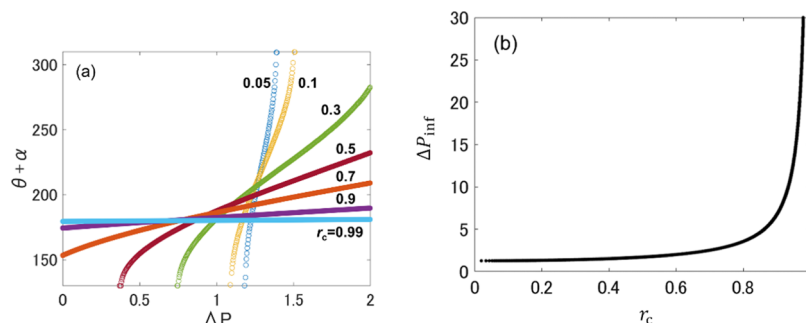
state where the crystal acted as a "plug" to prevent the melt from leaking.

It was difficult to identify the location of z_d because the interior of the die could not be directly observed during crystal growth. If z_c dropped owing to overheating and melt infiltration occurred, a melt leakage was observed when z_d reached the lower end of the die. The outflow continued until the pressure on the melt side became equal to either the inflow pressure of the through hole or the critical pressure of the droplets that were formed at the lower end of the die. When the cooling was sufficient and z_d was present inside the die, $r_c \approx r_d$ with the inflow of the melt under pressure despite a temporary narrowing of the crystal diameter. Figure 8 shows
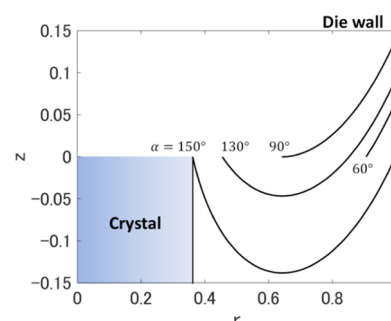

Figure 8. Capillary shapes for different r_c.

the meniscus shapes in a system composed of a crucible that is filled with an iridium melt, wherein the melt height and hole diameter are approximately 10 cm and 0.5 mm, respectively. Here, ΔP and θ were assumed to be 2.12 and 130°, respectively. The position of the lower end of the melt was depicted to be lower than z_c at a crystal thickness (r_c) of less than ≈0.65. Here, it was assumed that sufficient hysteresis existed at the triple point on the crystal side.

From the similarity with the Bridgman method, the dynamic stability criteria in the free-end condition at a low Bo number may be determined by applying the analytical equation that was derived by Duffar et al.[21]

$$\left(\frac{\partial \alpha_0}{\partial r}\right)_{r=r_c} = \frac{1}{2\sin\alpha}\left[\frac{2\cos\theta}{r_d} - \frac{p_h - p_c}{\gamma}\left(1 + \frac{r_d}{(r_d - e)^2}\right)\right]$$
$$< 0 \tag{5}$$

where $p_h - p_c$ is greater than or equal to 0 because the dewetting μ-PD method is generally applied in an open system.

Figure 7. (a) Dependence of $\alpha + \theta$ on ΔP in the free-end condition. (b) Variation of the melt infiltration pressure with the radius of the seed crystal.

Thus, the conditions for the dynamic stability are always satisfied when r_c is approximately equal to r_d.

There were no constraints by the inner wall in the conventional μ-PD method. Therefore, the melt drop, which was attributed to the instability of the meniscus or the transition from the fixed-end condition at the edge of the die to the free-end condition at the outer wall of the die, occurred under a high pressure. This prevented shape controllability. For the free-end condition, specifically in the case of $r_c \approx r_d$ in the dewetting μ-PD method, dynamic stability was guaranteed as long as (r_c, z_c) was within the die boundaries in the $z-r$ plot. The presence of (r_c, z_c) within the capillary hole in the $z-r$ plot was ensured by sufficient cooling and mechanical retention of the seed.

3.3. Transition between the Fixed-End and Free-End Conditions.
The fixed-end and free-end conditions in the dewetting μ-PD method were smoothly connected at the inner edge of the die. Depending on the pressure and position of the triple point on the crystal side, the following conditions were realized during the crystal growth:

(i) If $\Delta P < \Delta P_{inf}$, the fixed-end condition was considered. If the free-end condition existed initially, a transition to the fixed-end condition occurred.

(ii) If $\Delta P > \Delta P_{inf}$ and the gap width was less than the equilibrium gap width for the loaded pressure, the fixed-end condition was considered for the presence of z_c within the envelope starting from the edge of the die side; conversely, the free-end condition was considered for the presence of z_c outside the envelope.

(iii) If $\Delta P > \Delta P_{inf}$ and the gap width was greater than the equilibrium gap width for the loaded pressure, a transition from the fixed-end condition to the free-end condition with infiltration occurred.

The transition in the boundary condition occurred after melt infiltration during the actual growth of the crystal. This was attributed to the situation in point (iii), wherein the heat transfer through the crystal increased with the increase in crystal diameter. Consequently, z_c reached the envelope again owing to the increase in the heat transfer through the crystal. Thus, the fixed-end condition was obtained, as explained in point (ii).

3.4. Relation between the Capillary Shape and Angle Conditions for the Crystal Radius and Pressure.
It is not possible to observe the meniscus directly in the dewetting μ-PD method, which is the primary difference between the dewetting μ-PD method and conventional CST methods. Therefore, it was necessary to predict the internal state of the meniscus to optimize the crystal growth conditions. The determination of α, θ, and ΔP was necessary to obtain the solution of the Young–Laplace equation for a given Bo number. The α_{gr} for pure materials can be determined experimentally, and it has been measured for semiconductors, oxides, and certain pure metals;[33−35] however, the instances of such measurements are limited. Furthermore, no such measurements have been performed for iridium and ruthenium. It is difficult to determine the triple point for mixtures or incongruent melting systems, such as alloys, owing to the dynamic change of composition around the triple point. These changes can be attributed to segregation at the solidification interface and the formation of the Massey zone. Additionally, θ varies depending on the surface condition of the insulator, atmosphere, and dissolved impurities in the melt.

However, θ has a higher controllability than α. Furthermore, the value of θ can be greater than that predicted from the static contact angle owing to the presence of hysteresis. It was possible to observe r_c immediately after exposure outside the die during the crystal growth in the experiment, and ΔP was approximated from the melt height. The possible combinations of α and θ were limited using the relationship between ΔP and r_c. Thus, it was possible to predict the behavior of the capillary and provide guidance for controlling the crystal diameter and contact angle.

3.4.1. Fixed-End Condition. Figure 9 shows the relationship between ΔP and $\alpha + \theta$, in consideration with r_c, in the fixed-
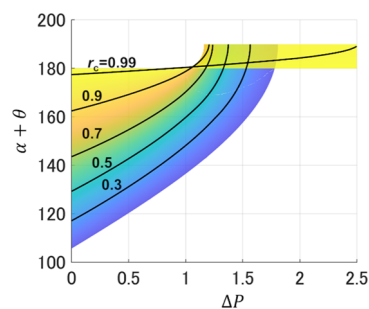

Figure 9. Relationship between ΔP and $\alpha + \theta$ in the fixed-end conditions. The color scale indicates the crystal radius, r_c.

end condition, wherein the Bo number and α are 0.0215 and 10°, respectively, with $\pi/2 \leq \theta \leq \pi$. A range of single-valued solutions for ΔP was obtained from this figure.

Two single-valued solutions were obtained in the region of $\Delta P = 1.2−1.8$. Furthermore, $r_c \approx r_d$ was achieved in the yellow region, and r_c was maximized at $\theta + \alpha < \pi$ in the low-pressure region below $\Delta P \approx 1.2$ and at $\theta + \alpha > \pi$ in the high-pressure region above $\Delta P \approx 1.2$. The relationship between ΔP and $\alpha + \theta$ was obtained for several values of r_c, denoted by solid lines in Figure 9. When r_c was similar to r_d, $\theta + \alpha$ was also similar to π in all the pressure regions.

3.4.2. Free-End Condition. Figure 10 shows the dependence of $\alpha + \theta$ on r_c and ΔP for a Bo number and α of 0.0215 and
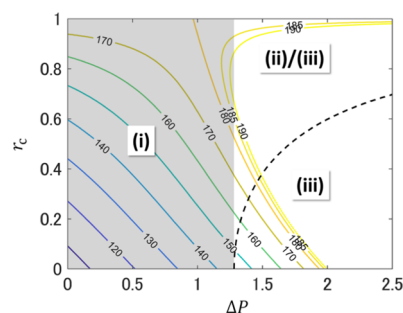

Figure 10. Pressure dependence of the crystal diameter. The dashed line shows the relationship between ΔP and r_c for $\alpha = 90°$.

15°, respectively, with $\pi/2 \leq \theta \leq \pi$. The contour line represents the $\alpha + \theta$ that was obtained under the assumption of the free-edge condition, and the black dotted line shows the critical infiltration pressure at $\theta = 130°$. Each region in the figure corresponds to a case of the aforementioned boundary conditions. The fixed-end condition existed in region (i), where no infiltration occurred. When the initial boundary condition was the free-end condition, a transition occurred in the fixed-
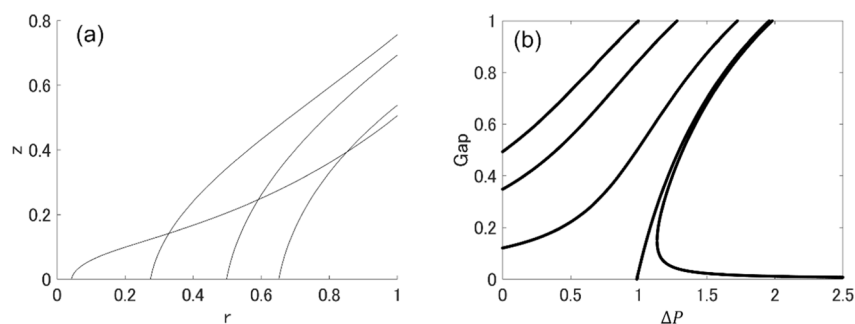
Figure 11. (a) Meniscus shapes at $\theta = 130°$ for several ΔP. (b) Pressure dependence of the gap width for different θ.
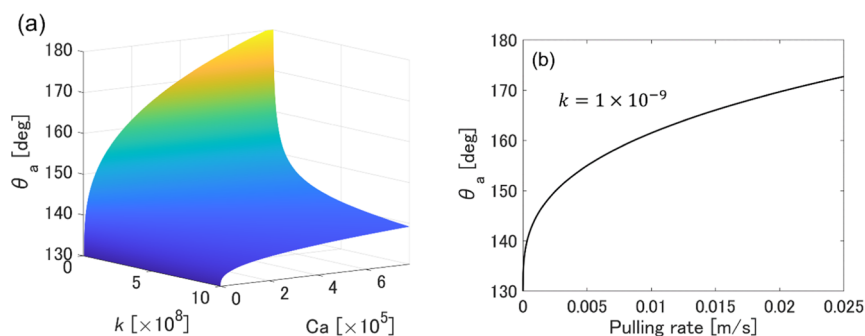

Figure 12. (a) Relationship between the capillary number Ca, the constant depending on the surface k, and the dynamic contact angle. (b) Relationship between the pulling rate and the dynamic contact angle in the case of $k = 9 \times 10^{-9}$.

region (i) to the fixed-end condition. The boundary condition in region (ii) was either the fixed-end or free-end condition, depending on the position of the solid−liquid interface. The contour lines in region (iii) (inside the dashed line) were hypothetical owing to the penetration of the melt into the gap. The penetration stopped at the line diameter on the dashed line, which corresponded to a certain pressure, under sufficient cooling. However, r_c could undergo dynamic variations within the range as the crystal was pulled down because the condition, $\alpha = \alpha_{gr}$, was not guaranteed. Furthermore, r_c did not exhibit consistent dynamic stability because the gap width was not negligible.

Figure 11a shows the meniscus shapes at $\theta = 130°$ in the free-end condition. The meniscus showed a minimum dimensionless gap width of 0.348 at $\Delta P = 0$ in the region of $\Delta P = 0-1.2$. Figure 11b shows the dependence of the gap width on ΔP. The plot at $\theta = 130°$ corresponds to the gap width that is obtained for the meniscus in Figure 11a, and the gap width was minimum at $\Delta P = 0$. The gap width tended to increase with the increase in ΔP in the region at which $\theta + \alpha < \pi$. This indicated that when θ was high and $\theta + \alpha$ was close to π, the crystal diameter approached the hole diameter. However, two solutions were obtained within the region at which $\theta + \alpha > \pi$. The gap width increased with the increase in pressure in the region where the gap width was greater than the inflection point. Similarly, the gap width decreased with the increase in the pressure in the region where the gap width was less than the inflection point.

The gaps with the lowest width for a given pressure were obtained for $\Delta P \leq 1$ at the minimum value of $|\theta + \alpha - \pi|$ (Figure 11b). Two solutions with concave and convex menisci were obtained for $\Delta P = 1-1.8$. The region of the concave meniscus contained small gaps, with the smallest gap at the minimum value of $|\theta + \alpha - \pi|$.

3.4.3. Influences of the Contact Angle. There were two stable regions, $\theta + \alpha \leq \pi$ and $\theta + \alpha > \pi$, at which $r_c \approx r_d$ was achieved. It was experimentally determined that the growth of iridium and ruthenium crystals at $r_c \geq 0.99$ was stable and sustainable in both pressure regimes. Although $\theta + \alpha \approx \pi$ was required to achieve $r_c \geq 0.99$, the statically observed equilibrium contact angles for iridium and ruthenium with the oxides were approximately 130°. The experimental determination of α_{gr} is not easy; however, it is known to be in the range of 0−30°. Even by considering $\alpha_{gr} = 30°$, the sum of θ and α would be merely 160°, which is still less than 180°. Therefore, it was necessary to consider the existence of a mechanism by which θ could be dramatically increased when compared to its static value.

θ can be higher than the equilibrium contact angle in the fixed-end condition owing to the hysteresis of the contact angle. Conversely, θ is often approximated as the equilibrium contact angle in the free-end conditions of slow crystal growth. It has been mentioned in previous studies that oxidation of the surface can induce an increase in θ.[36] However, iridium and ruthenium are not oxidized in a pure Ar atmosphere; furthermore, the oxides are highly volatile and do not form a film on the surface. Therefore, a substantial advancing contact angle was expected even in the free-end conditions.

The hysteresis of the contact angle was observed even on smooth surfaces. It was also difficult to theoretically predict the absolute values of the advancing and receding contact angles because these angles exhibited a significant variation depending on the state of the solid surface.[37] The dynamic contact angle increases with the flow velocity at a relatively low Ca number[38] and can be determined using the following expression formulated by Tanner[39,40]

$$Ca = \frac{v\mu}{\gamma} = k(\theta_e - \theta_a)^3 \tag{6}$$

where θ_e is the equilibrium contact angle, v is the flow velocity, μ is the kinematic viscosity coefficient, and k is a constant that is obtained experimentally and depends on the solid surface; for example, $k = 9 \times 10^{-9}$ for water on acrylic.[38] Figure 12a shows the value of k and the advancing contact angle with respect to the fluid velocity (approximated to the pulling rate) at $\theta_e = 132°$. Figure 12b shows the pulling rate dependence of θ_a for a certain value of k. This relationship suggested that in the speed range below 100 mm min^{-1}, a rapid increase in θ_a occurred with an increase in the pulling-down speed.

The dewetting μ-PD method not only exhibited a low gap width between the melt and wall but also showed a temperature gradient greater than 100 K mm^{-1} in the vertical direction and a unidirectional flow of the melt in the vicinity of the triple point. Therefore, the gas molecules inside the die were always expelled out of the die due to the thermal motion and entrainment flow that were associated with the pulling-down technique. Achieving $r_c \approx r_d$ implied that the increase in ΔP corresponded directly to the increase in θ_a. Moreover, $\Delta P > 1$ was achieved with a 10% decrease in pressure from the atmospheric pressure for pure iridium with a crystal diameter of 0.5 mm even if the hydrostatic pressure owing to the melt height was 0. It was experimentally and reproducibly observed that the control of the crystal size became difficult in vacuum even at identical pulling-down rates as those in the dewetting μ-PD method. This indicated the decrease in θ_a with the decrease in θ_e. A detailed evaluation of the effects of pressure fluctuation and the pulling-down rate on θ_a is expected to be performed in future experiments and from the viewpoint of fluid dynamics.

3.4.4. Scope of the Applications of the Dewetting μ-PD Method. The results indicated that it was necessary to achieve $\theta + \alpha \approx \pi$ to realize shape controllability with $r_c \approx r_d$ in the dewetting μ-PD method. It was difficult to achieve $r_c \approx r_d$ for materials with low α_{gr}, such as Au ($\alpha_{gr} = 0°$). This can be attributed to the attainment of the highest r_c near the envelope apex even in the fixed-end condition at θ_e of approximately 130° between a typical metal and a ceramic. Such systems are susceptible to dynamic instabilities owing to minor fluctuations. Therefore, shape controllability in these cases can be achieved by the conventional μ-PD method or the edge-defined film-fed growth method using a die with high wettability. When α is moderate, the shape controllability with $r_c \approx r_d$ can be obtained in the presence of a combination of ideal insulation materials. It can also be realized with the attainment of $\theta + \alpha_{gr} \approx \pi$ owing to a substantial increase in θ with the formation of oxide films. Conversely, a high θ in systems with high α_{gr} is likely to result in $\theta + \alpha > \pi$. This induces a decrease in the crystal diameter, especially in the low ΔP region. The shape controllability in such systems can be achieved by decreasing θ, which involves controlling the temperature in the fixed-end condition, where no melt infiltration occurs. Empirically, a material with a high contact angle is selected in the dewetting μ-PD method because $\alpha_{gr} + \theta$ is less than π for a typical combination of materials.

α_{gr} is not uniquely determined for alloys and mixed salts that exhibit a solidus and liquidus. The solidification phenomena in such systems require a separate discussion. However, there are multiple examples of investigations on Al-based alloys,[32] wherein shape control has been successfully achieved with iridium-40 wt. % Rh.[15] Therefore, the possibility of practical capillary analyses and predictions using reasonable approximations has been demonstrated.

4. CONCLUSIONS

This study demonstrated a specific μ-PD method, known as the dewetting μ-PD method, for low-wettability systems. The achievement of shape controllability for the system, where the solid−liquid interface was located in the hole of the die and was not visible from outside, was investigated by estimating the capillary shape using the Young−Laplace equation.

The transition from the fixed-end condition to the free-end condition in the dewetting μ-PD method was based on the pressure that was applied to the capillary. The critical pressure in the through hole was considered as the threshold pressure for the melt infiltration; however, the mechanical holding of the crystals facilitated the crystal growth at pressures greater than the threshold pressure. The relationship between the crystal radius and pressure for $\alpha = 90°$ was utilized to determine the threshold pressure for the melt infiltration in this study. The critical pressure for $\theta = 130°$ increased significantly from the region where the dimensionless crystal radius exceeded 0.8.

The melt front at the die wall maintained a contact angle of θ in the free-end condition, and the dynamic stability of the dewetting μ-PD method in an open system was investigated based on similarities with the Bridgman method. The crystal size depended on the applied pressure. When the fixed-end condition was achieved at the upper edge of the die or at the inner die wall within the hysteresis, dynamic stability was achieved in the region of the die side of the envelope apex for melts having a low Bo number. The effect of gravity was negligible in this region. The change in the height of the triple point on the crystal side was determined by the temperature field and induced a variation in θ. Thus, the crystal diameter was regulated in the fixed-end condition. The necessary condition to obtain a capillary with the maximum diameter for a given pressure was to minimize $|\theta + \alpha - \pi|$ for both the boundary conditions.

The equilibrium contact angles of iridium and ruthenium with the ceramics were approximately 130°. The experimental results suggested that the achievement of $\theta + \alpha \approx \pi$ for iridium and ruthenium was attributed to the high advancing contact angle because the crystal diameters were approximately equal to the inner diameter of the die. Opportunities exist for future research on the measurement of α_{gr} and the investigation of mechanisms to increase the advancing contact angle in the dewetting μ-PD method.

Although the present study was carried out for pure materials, for which α_{gr} was uniquely determined, it is necessary to provide an appropriate approximation of α_{gr} for mixed systems, such as alloys, wherein the α_{gr} varies dynamically due to segregation at the solidification interface or the formation of a massy zone.

■ AUTHOR INFORMATION

Corresponding Author

Rikito Murakami − *Department of Metallurgy, Graduate School of Engineering and Institute for Materials Research, Tohoku University, Sendai 980-8577, Japan; Department of Research and Development, C&A Corporation, Sendai 980-0845, Japan;* ⓘ orcid.org/0000-0002-2825-4243; Email: r_murakami@imr.tohoku.ac.jp

Authors

Katsunari Oikawa − *Department of Metallurgy, Graduate School of Engineering, Tohoku University, Sendai 980-8577, Japan*

Kei Kamada − *Department of Research and Development, C&A Corporation, Sendai 980-0845, Japan; Institute for Materials Research, Tohoku University, Sendai 980-8577, Japan*

Akira Yoshikawa − *Department of Research and Development, C&A Corporation, Sendai 980-0845, Japan; Institute for Materials Research and New Industry Creation Hatchery Center, Tohoku University, Sendai 980-8577, Japan*

Complete contact information is available at:
https://pubs.acs.org/10.1021/acsomega.0c05913

Notes

The authors declare no competing financial interest.

■ ABBREVIATIONS

CST, Capillary shaping technology; YSZ, yttria-stabilized zirconia

■ REFERENCES

(1) Duffar, T.; Sylla, L. Vertical Bridgman Technique and Dewetting. In *Crystal Growth Processes Based on Capillarity: Czochralski, Floating Zone, Shaping and Crucible Techniques*; Duffar, T., Ed.; Wiley: Chichester, 2010.

(2) Yoshikawa, A.; Nikl, M.; Boulon, G.; Fukuda, T. Challenge and study for developing of novel single crystalline optical materials using micro-pulling-down method. *Opt. Mater.* **2007**, *30*, 6−10.

(3) Furukawa, Y.; Kitamura, K.; Suzuki, E.; Niwa, K. Stoichiometric LiTaO$_3$ single crystal growth by double crucible Czochralski method using automatic powder supply system. *J. Cryst. Growth* **1999**, *197*, 889−895.

(4) Nikl, M.; Yoshikawa, A.; Kamada, K.; Nejezchleb, K.; Stanek, C. R.; Mares, J. A.; Blazek, K. Development of LuAG-based scintillator crystals - a review. *Prog. Cryst. Growth Charact. Mater.* **2013**, *59*, 47−72.

(5) Akselrod, M. S.; Bruni, F. J. Modern trends in crystal growth and new applications of sapphire. *J. Cryst. Growth* **2012**, *360*, 134−145.

(6) Yoshikawa, A.; Novoselov, A. High-Melting Rare-Earth Sesquioxides: Y$_2$O$_3$, Lu$_2$O$_3$, and Sc$_2$O$_3$. In *Shaped Crystals: Growth by Micro-Pulling-Down Technique*; Fukuda, T., Chani, V. I., Ed.; Springer: New York, 2007.

(7) Kamada, K.; Murakami, R.; Kochurikhin, V. V.; Luidmila, G.; Jin Kim, K.; Shoji, Y.; Yamaji, A.; Kurosawa, S.; Ohashi, Y.; Yokota, Y.; Yoshikawa, A. Single crystal growth of submillimeter diameter sapphire tube by the micro-pulling down method. *J. Cryst. Growth* **2018**, *492*, 45−49.

(8) Murakami, R.; Kamada, K.; Hatakeyama, S.; Ueno, K.; Ueno, Y.; Tadokoro, T.; Shoji, Y.; Kurosawa, S.; Yamaji, A.; Ohashi, Y.; Yoshino, M.; Yokota, Y.; Yoshikawa, A. Single crystal growth and luminescent properties of Tb doped GdTaO4 by the μ-pulling down method. *Opt. Mater.* **2019**, *87*, 94−97.

(9) Kim, K. J.; Jouini, A.; Yoshikawa, A.; Simura, R.; Boulon, G.; Fukuda, T. Growth and optical properties of Pr, Yb-codoped KY$_3$F$_{10}$ fluoride single crystals for up-conversion visible luminescence. *J. Cryst. Growth* **2007**, *299*, 171−177.

(10) Yoshikawa, A.; Satonaga, T.; Kamada, K.; Sato, H.; Nikl, M.; Solovieva, N.; Fukuda, T. Crystal growth of Ce: PrF$_3$ by micro-pulling-down method. *J. Cryst. Growth* **2004**, *270*, 427−432.

(11) Oikawa, K.; Shoji, T.; Anzai, K. Effect of Zr addition on magnetostriction of Tb-Dy-Te alloys prepared by micro-pulling-down method. *Mater. Sci. Forum* **2014**, *783−786*, 2497−2502.

(12) Yokota, Y.; Nihei, T.; Tanaka, K.; Sakairi, K.; Chani, V.; Ohashi, Y.; Kurosawa, S.; Kamada, K.; Yoshikawa, A. Fabrication of metallic fibers with high melting point and poor workability by unidirectional solidification. *Adv. Eng. Mater.* **2018**, *20*, 1700506.

(13) Yoshikawa, A.; Sutou, Y. Metal Alloy Fibers. In *Shaped Crystals*; Fukuda, T., Chani, V. I., Eds.; Springer-Verlag: New York, 2007; pp 331−334.

(14) Ishikawa, H.; Sutou, Y.; Omori, T.; Oikawa, K.; Ishida, K.; Yoshikawa, A.; Umetsu, R. Y.; Kainuma, R. Pd−In−Fe shape memory alloy. *Appl. Phys. Lett.* **2007**, *90*, 261906.

(15) Murakami, R.; Kamada, K.; Shoji, Y.; Yokota, Y.; Yoshino, M.; Kurosawa, S.; Ohashi, Y.; Yamaji, A.; Yoshikawa, A. Fabrication of flexible Ir and Ir-Rh wires and application for thermocouple. *J. Cryst. Growth* **2018**, *487*, 72−77.

(16) Lan, C. W.; Uda, S.; Fukuda, T. Theoretical analysis of the micro-pulling-down process for Ge$_x$Si$_{1-x}$ fiber crystal growth. *J. Cryst. Growth* **1998**, *193*, 552−562.

(17) Samanta, G.; Yeckel, A.; Daggolu, P.; Fang, H.; Bourret-Courchesne, E. D.; Derby, J. J. Analysis of limits for sapphire growth in a micro-pulling-down system. *J. Cryst. Growth* **2011**, *335*, 148−159.

(18) Tatarchenko, V. A. *Shaped Crystal Growth*; Kluwer Academic Publishers Group: Dordrecht, 1993.

(19) Duffar, T.; Dusserre, P.; Giacometti, N. Growth of GaSb single crystals by an improved dewetting process. *J. Cryst. Growth* **2001**, *223*, 69−72.

(20) Duffar, T.; Dusserre, P.; Picca, F.; Lacroix, S.; Giacometti, N. Bridgman growth without crucible contact using the dewetting phenomenon. *J. Cryst. Growth* **2000**, *211*, 434−440.

(21) Duffar, T.; Boiton, P.; Dusserre, P.; Abadie, J. Crucible de-wetting during Bridgman growth in microgravity. II. smooth crucibles. *J. Cryst. Growth* **1997**, *179*, 397−409.

(22) Schweizer, M.; Volz, M. P.; Cobb, S. D.; Vujisic, L.; Motakef, S.; Szoke, J.; Szofran, F. R. Stability of detached-grown germanium single crystals. *J. Cryst. Growth* **2002**, *237−239*, 2107−2111.

(23) Balint, S.; Epure, S. Non-lyapunov type stability in a model of the dewetted Bridgman crystal growth under zero gravity conditions. *Microgravity Sci. Technol.* **2011**, *23*, 49−58.

(24) Mazuruk, K.; Volz, M. P. Static stability of menisci in detached Bridgman growth. *Phys. Fluids* **2013**, *25*, 094106.

(25) Volz, M. P.; Mazuruk, K. Existence and shapes of menisci in detached Bridgman growth. *J. Cryst. Growth* **2011**, *321*, 29−35.

(26) Strutt, J. W. On the Capillary Phenomena of Jets. *Scientific Papers*; Cambridge University Press: Cambridge, 1899; pp 377−395.

(27) Bardsley, W.; Frank, F. C.; Green, G. W.; Hurle, D. T. J. The meniscus in Czochralski growth. *J. Cryst. Growth* **1974**, *23*, 341.

(28) Properties of the Elements and Inorganic Compounds. In *Handbook of Chemistry and Physics*; Lide, D. R., Frederikse, H. P. R., Eds.; CRC Press: Boca Raton, 1997.

(29) Ishikawa, T.; Paradis, P.-F.; Fujii, R.; Saita, Y.; Yoda, S. Thermophysical property measurements of liquid and supercooled iridium by containerless methods. *Int. J. Thermophys.* **2005**, *26*, 893−904.

(30) Kinisarin, M. M.; Berezin, B. Y.; Gorina, N. B.; Kats, S. A.; Polyakova, V. P.; Savitskii, E. M.; Chekhorsko, V. A. Melting point of ruthenium. *Teplofiz. Vys. Temp.* **1974**, *12*, 1309−1310.

(31) Paradis, P.-F.; Ishikawa, T.; Yoda, S. Thermophysical properties of liquid and supercooled ruthenium measured by noncontact methods. *J. Mater. Res.* **2004**, *19*, 590−594.

(32) Tatartchenko, V. A. Crystal Growth Process Based on Capillarity. In *Crystal Growth Processes Based on Capillarity: Czochralski, Floating Zone, Shaping and Crucible Techniques*; Duffar, T., Ed.; Wiley: Chichester, 2010.

(33) Surek, T.; Chalmers, B. The direction of growth of the surface of a crystal in contact with its melt. *J. Cryst. Growth* **1975**, *29*, 1−11.

(34) Wenzl, H.; Fattah, A.; Gustin, D.; Michelcic, M.; Uelhoff, W. Measurements of the contact angle between melt and crystal during Czochralski growth of gallium and germanium. *J. Cryst. Growth* **1978**, *43*, 607.

(35) Glebovsky, V. G.; Semenov, V. N.; Lomeyko, V. V. The characteristic features of growth and the real structure of tungsten tube crystals. *J. Cryst. Growth* **1989**, *98*, 487.

(36) Sylla, L.; Paulin, J. P.; Vian, G.; Garnier, C.; Duffar, T. Effect of residual gaseous impurities on the dewetting of antimonide melts in fused silica crucibles in the case of bulk crystal growth. *Mater. Sci. Eng., A* **2008**, *495*, 208−214.

(37) Semenov, S.; Starov, V.; Rubio, R. G. Contact Angle Prediction. In *Droplet Wetting and Evaporation: From Pure to Complex Fluids*; Brutin, D., Ed.; Academic Press: San Diego, 2015.

(38) Hoffman, R. L. A study of the advancing interface. I. Interface shape in liquid-gas systems. *J. Colloid Interface Sci.* **1975**, *50*, 228−241.

(39) Kikuta, D.; Aoki, T.; Matsushita, S. A simulation of droplets with dynamic contact angles running down on a flat slope. *JSFM CFD33 C11-5*, 2019; pp 1−6.

(40) Tanner, L. H. The spreading of silicon oil drops on horizontal surfaces. *J. Phys. D: Appl. Phys.* **1979**, *12*, 1473.